Fabric Investigation of Natural Sensitive Clay from 3D Nano- And Microtomography Data

ASCE

Fabric Investigation of Natural Sensitive Clay from 3D Nano- and Microtomography Data

Georgios Birmpilis, Ph.D.[1]; Amir Saeid Mohammadi, Ph.D.[2]; Julie Villanova, Ph.D.[3]; Elodie Boller[4]; Edward Ando, Ph.D.[5]; and Jelke Dijkstra[6]

Abstract: The three-dimensional (3D) fabric in natural sensitive clay is quantified from a combination of high resolution nano and microtomographies, scanning electron microscopy, and dynamic light scattering. Although the speckle arising from clay particles and the pores they enclose is discerned in the nanotomography data and compare well with scanning electron microscopy (SEM) images on the same clay, the individual platelet-shaped clay particles cannot be segmented for subsequent quantitative analysis. Regardless, a very wide range of particle sizes—0.1–300 μm—was detected using the current state-of-the-art in imaging and postprocessing. The measured aspect ratios range was 2.5 ± 1; hence, the particles identified were not clay platelets but, rather, mechanically weathered particles embedded in the clay matrix. Furthermore, the smaller particle sizes <80 μm presented a consistent 22–23° deviation in orientation from the horizontal plane, whereas the larger fractions had a horizontal orientation. The latter finding agrees well with prior findings on the inclination of the clay minerals using small angle X-ray scattering. Finally, the measured mean particle size of 450 nm determined from the nano data is corroborated by an independent determination of particle sizes using dynamic light scattering. **DOI: 10.1061/(ASCE)EM.1943-7889.0002044.**

Author keywords: X-ray computed tomography; Natural sensitive clay; Fabric; Image processing.

Introduction

The emerging hydromechanical response of natural clays at an engineering scale (macro) is governed at the materials science scale (micro); that is, the microstructural effects arising from the particle assembly and interparticle interactions within the clay lead to a complex hydromechanical response observed at the engineering scale. Burland (1990) denoted the microstructural effects that are observed in a wide range of soils as the structure of soils: a combination of fabric and the (apparent) bonding between the particles (Leroueil and Vaughan 1990). In the following, the bonding is interpreted as the nonfrictional interparticle forces in the clay (Santamarina 2003), whereas the fabric describes the distribution of the directional data, e.g., orientation of clay particles, void space, and/or contacts (Ken-Ichi 1984). Methods from materials science, such as scanning and transmission electron microscopy (SEM/TEM), mercury intrusion porosimetry (MIP), and wide or small angle X-ray or neutron scattering (W/SAXS, SANS) (e.g., Glatter and Kratky 1982; Toer and Reimer 1998; Giesche 2006) have been introduced in geomechanics to further probe clays at microscale despite their inherent limitations for use in fine-grained materials (Yao and Liu 2012; Deirieh et al. 2018). The ultimate aim is to link the micro and macro response (e.g., Pusch 1970; Delage and Lefebvre 1984; Djéran-Maigre et al. 1998; Hicher et al. 2000; Ringdal et al. 2010; Delage 2010; Hattab and Fleureau 2011; Hattab et al. 2013; Suuronen et al. 2014; Wensrich et al. 2018; Birmpilis et al. 2019; Cotecchia et al. 2019; Delage and Tessier 2021; Abed and Sołowski 2020; Schuck et al. 2020; Dor et al. 2020; Zhao et al. 2020). Regardless of the experimental method, either a bulk response of the complete sample volume (MIP, W/SAXS, SANS), a two-dimensional (2D) map of the integrated response along the transmitted X-ray/electron beam (scanning W/SAXS and TEM), or a 2D surface profile (with a certain depth of view) is obtained (SEM). Therefore, none of the methods are truly three-dimensional (3D), which hampers the characterization of the complex spatially organized dense systems of polydisperse particles that are present in natural clays.

X-ray computed tomography (XCT) overcomes the aforementioned limitations because it obtains 3D image data of the sample under test and is already used for characterization and process monitoring of fine-grained geomaterials, such as clay and clayrock (e.g., Viggiani et al. 2004; Hemes et al. 2015; Wang et al. 2017; Stavropoulou et al. 2020). In these studies, spatial heterogeneities from features that are substantially larger than the particle size of individual clay platelets were investigated, such as the characteristics of macro pores, crack formation, or continuum scale deformations devised from an evolving (natural) speckle pattern during a

[1]Research Engineer, Dept. of Architecture and Civil Engineering, Chalmers Univ. of Technology, Gothenburg SE-41296, Sweden (corresponding author). ORCID: https://orcid.org/0000-0002-8353-693X. Email: georgios.birmpilis@chalmers.se; geobir@chalmers.se

[2]Research Engineer, Dept. of Architecture and Civil Engineering, Chalmers Univ. of Technology, Gothenburg SE-41296, Sweden. ORCID: https://orcid.org/0000-0002-4600-773X. Email: saamir@chalmers.se

[3]Beamline Scientist, ESRF-The European Synchrotron, 71 Ave. des Martyrs, Grenoble 38000, France. ORCID: https://orcid.org/0000-0001-6157-2289. Email: julie.villanova@esrf.fr

[4]Engineer, ESRF-The European Synchrotron, 71 Ave. des Martyrs, Grenoble 38000, France. Email: boller@esrf.fr

[5]Research Engineer, Laboratory 3SR (SOLS, SOLIDES, STRUCTURES, RISQUES), French National Centre for Scientific Research, Graduate Schools of Engineering and Management Univ. Grenoble Alpes, Laboratory 3SR, F38000, France. ORCID: https://orcid.org/0000-0001-5509-5287. Email: edward.ando@3sr-grenoble.fr

[6]Professor, Dept. of Architecture and Civil Engineering, Chalmers Univ. of Technology, Gothenburg SE-41296, Sweden. Email: jelke.dijkstra@chalmers.se

Note. This manuscript was submitted on February 21, 2021; approved on September 17, 2021; published online on December 7, 2021. Discussion period open until May 7, 2022; separate discussions must be submitted for individual papers. This paper is part of the ***Journal of Engineering Mechanics***, © ASCE, ISSN 0733-9399.

mechanical test. Submicron spatial resolution is required for the study of fine-grained soils, such as natural clays for which the largest dimension is on the order of $O(\mu m)$ (Mitchell and Soga 2005). Recently, synchrotron-based imaging instruments, including at the beam lines ID16 and ID19 of the European Synchrotron (ESRF) (Martínez-Criado et al. 2016; Boller et al. 2017) used in this study, have started to attain the required submicron spatial resolutions. Furthermore, the favorable attributes of a synchrotron X-ray source allow the exploitation of phase contrast mechanisms (i.e., Cloetens et al. 1999; Paganin et al. 2002), which is essential for imaging natural clays that generally have poor absorption contrast (Birmpilis 2020).

The importance of the fabric on the emerging mechanical response of geomaterials is undisputed. Experimental quantification of fabric started with 2D plane stress experiments on photoelastic discs (Oda and Konishi 1974) and have since progressed to the study of more complex assemblies of (natural) granular materials using laboratory- or synchrotron-based XCT (Imseeh et al. 2018; Rorato et al. 2020; Wiebicke et al. 2020; Zhao et al. 2021). For the latter, directional measurements of fabric are based on geometrical features extracted from the 2D and/or 3D image data. Alternatively, the output from discrete element modeling has been used in the absence of experimental data (e.g., Yimsiri and Soga 2010; Zhao and Guo 2013; Kuhn et al. 2015). In coarse grained materials, the orientation of contact normal vectors, void vectors, and branch vectors or simply the orientation of the primary axis of the particle (e.g., Bathurst and Rothenburg 1990; Fonseca et al. 2013; Kuhn et al. 2015) are all used as input for the fabric tensor in contemporary continuum models for coarse grained materials (Wang et al. 2020). In contrast, for clay samples, the particle orientations are most often extracted as a measure for fabric from microscopy data (e.g., Cotecchia et al. 2019; Zhao et al. 2020), W/SAXS (Birmpilis et al. 2019), or SANS (Wensrich et al. 2018). However, the continuum models starting from the fabric measured experimentally at the particle scale are still in their infancy.

In this work, the 3D fabric, that is, the particle directions for different size fractions, is quantified experimentally from unprecedented high resolution nano- and microtomography data on undisturbed samples of a natural sensitive clay from Sweden.

Measurement Methods

ISP Method

The integral suspension pressure (ISP) method (Durner et al. 2017) was utilized to obtain the distribution of the mass fractions of the natural clay tested. ISP is a column sedimentation method in which Stokes' law is applied to determine particle sizes related to the measured temporal change of the suspension pressure that results from the reduction of the particle concentration during sedimentation at a specific depth. The sample was prepared for the determination of the particle size distribution by wet sieving and the sedimentation method according to SS-ISO 11277:2020. Amendments in the procedure were made based on the recommendations for the use of the PARIO soil particle analyzer (METER Group, Pullman, Washington) (Gee and Or 2002). In particular, all particles <2 mm were removed prior to the treatment of the sample by sieving. After the organic content was measured to be 4% [loss on ignition: SS-EN 15935:2012 (SIS 2012)], the sample was treated for organic matter destruction [SS-ISO 11277:2020 (SIS 2020)]. Soluble salts were removed through washing by centrifuge drainage for 15 min at a relative centrifugal force (RCF) of 400 g [SS-ISO 11277:2020 (SIS 2020)] until the measured electrical conductivity was 2.1 mSm^{-1} (far below the limit of 40 mSm^{-1}). For chemical dispersion, sodium hexametaphospate was used following Gee and Or (2002), and physical dispersion was achieved by using an horizontal orbital shaking table at 125 min^{-1} overnight. The sedimentation measurement lasted 12 h, and the suspension was subsequently sieved using the wet sieving method to obtain the data for the larger fractions in the range of 63 $\mu m < d_{particle} < 2$ mm, directly after the measurement [SS-ISO 11277:2020 (SIS 2020)].

Dynamic Light Scattering

Dynamic light scattering (DLS) [ISO 22412:2017 (ISO 2017)] is commonly applied for the particle size analysis of nanoparticles. DLS is based on characterizing the Brownian motion of dispersed particles in a solvent. The magnitude of the motion is linked to the particle size, for which large particles move less than smaller particles. A monochromatic laser source incident on the sample is scattered by the particles in suspension, and the light intensity emergent from the sample at a specific angle is recorded over time. Subsequently, the intensity fluctuations of the signal, which resulted from the Brownian motion of the suspended particles, are used to correlate the size distribution from this periodic signal. An analytic overview of the method and its applications is presented in Stetefeld et al. (2016). The measurements were conducted using an Anton Paar Litesizer 500 (Anton Paar GmbH, Graz, Austria) particle size analyzer.

The samples were obtained from the supernatant of the sedimentation process. One sample was diluted to 0.01% w/v (g of soil per ml of the solution), and another sample was filtered first using a 2.5-μm filter. Both samples were sonicated for 15 min prior to the measurement to prevent aggregation of the particles.

Scanning Electron Microscopy

SEM is a well-established method for imaging the microstructure in (natural) clays. The morphological topography of a sample is quantified by scanning the surface with a focused electron beam. The SEM images were obtained using a FEI Quanta 200 FEG SEM at the Chalmers Materials Analysis Laboratory (CMAL). Thin slices of the clay sample (1 mm) were obtained by wire cutting and subsequently freeze-dried prior to the measurement. The samples were frozen at −20°C for 48 h. Thereafter, they were gradually dried under vacuum at room temperature for 12 h. Doing so preserves the structure of the clay sample when mounted in the vacuum chamber of the SEM instrument. After freeze drying, additional fractures were made to reveal the internal surfaces parallel to the consolidation direction of the clay deposit (vertical), that were unaffected from the wire cutting of the test specimen. These opened fractures were selected for subsequent SEM scanning. The measurements were acquired in high vacuum mode to achieve the highest resolution. For imaging with the back-scatter detector, a 15-kV beam was used.

Microtomography

X-ray computed tomography (XCT) is a noninvasive 3D imaging technique based on the acquisition and reconstruction of a series of 2D radiographic projections taken of a sample at different rotation angles. Measurements were made at the ID19 microtomography beamline at ESRF (Boller et al. 2017). High resolution scans required a smaller and high intensity beam of 93 keV. The camera carousel equipped with two PCO edge scientific CMOS cameras, and multiple objectives allowed selection among different optical magnifications (1X, 5X, and 20X), resulting in the following pixel sizes: 6.5, 1.3, and 0.3 μm. The scans at the lowest magnification used a 68-keV beam, and 2,000 projections were collected for each scan. In contrast, for the highest magnification, a 93-keV beam and 2,000 projections were used. To be noted is that for all

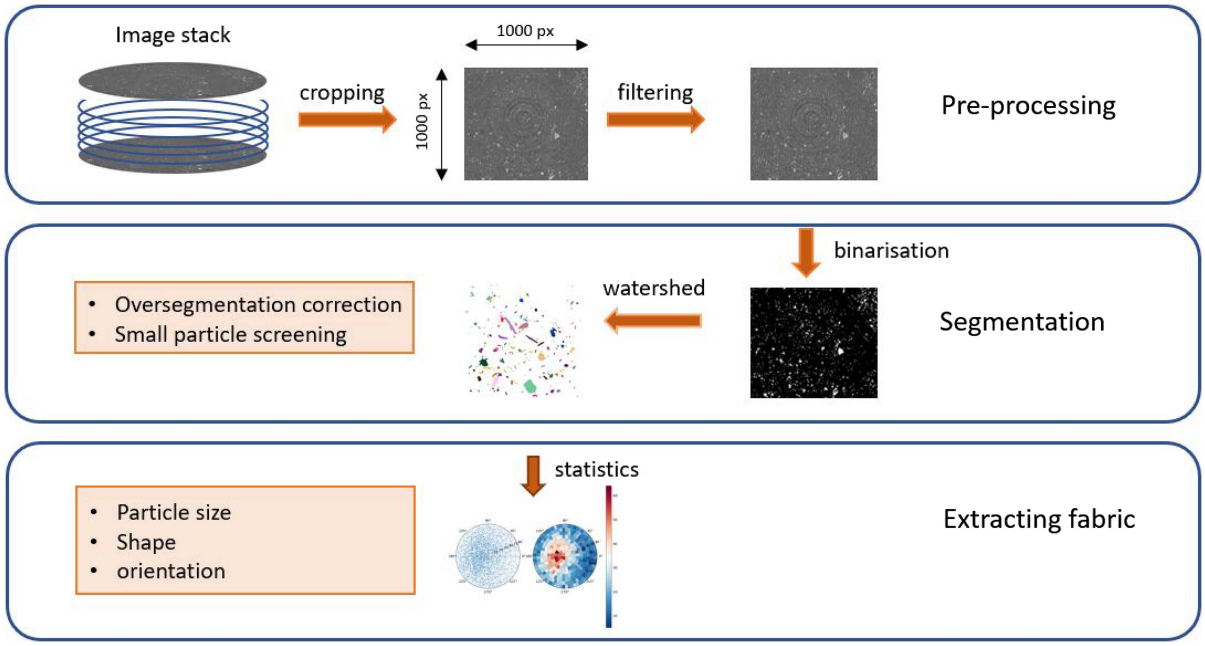

Fig. 1. Schematic overview of analysis of image data.

magnifications, the field of view (FoV) was smaller than the actual sample size, hence only covering a central subvolume within the clay sample.

The 10-mm diameter and 20-mm tall cylindrical sample was cored from a larger STII sample tube retrieved from the Utby test site in Sweden. The sample was mounted in the XCLAY miniature triaxial apparatus (Birmpilis 2020) to control the stresses, avoid loss of water, and monitor the porewater pressures during the scan. In all cases, the 3D data are reconstructed from the projections using parallel filtered back-projection with Paganin phase retrieval with a δ/β ratio of 500 (Paganin et al. 2002) using the ESRF reconstruction software PyHST2 (Mirone et al. 2014). This reconstruction technique retrieves phase contrast from the data using a fixed sample-detector position at the expense of a small loss in image sharpness.

Nanotomography

Although the ID19 microtomography beamline offers already impressive imaging capabilities, higher spatial resolutions are required to capture the smallest features in the clay. Therefore, the nanoscale imaging instrument at the ID16B beam line (Martínez-Criado et al. 2016) of ESRF was used to capture the nano features in the natural clay sample. This instrument requires miniature samples; hence, the natural clay was sampled into glass capillaries with 300-μm diameter and 10-μm wall thickness that were sealed at both ends with grease paste. In such a way, the clay sample maintained constant water content during the scan. The magnified phase contrast imaging technique used at ID16B is in-line holotomography (Cloetens et al. 1999), through which each nanotomographic scan consists of four tomographies taken at different sample-detector distances. The measurements were performed using a beam with an energy of 29.6 keV. For each scan, 3,009 projections with a pixel size of 25 nm and a FoV of 64 × 54 μm were recorded over 360° using a PCO edge 5.5 scientific CMOS camera with an acquisition time of 400 ms per projection. The 3D volumes were obtained after a two-step data processing procedure. First, the phase retrieval calculation was done using an in-house developed Octave script (Cloetens et al. 1999) with an iterative calculation based on a Paganin-like approach (Paganin et al. 2002) and δ/β of 190, where δ = refractive-index increment and β = absorption index. In the second step, the reconstruction was performed using a filtered back projection with the ESRF reconstruction software PyHST2 (Mirone et al. 2014).

Analyses of Image Data

The product of the acquisition and reconstruction from the nano and microtomographies, as described in the previous subsections, are 3D images (stacks of 2D images) representing a scalar "CT-value" as a rescaled greyscale quantity, approximately proportional to the local X-ray attenuation. The software used to process the data was the open-source code Fiji (ImageJ) (Schindelin et al. 2012) and Python-based scripts for further image analysis, as elaborated in the following subsections. A specific processing workflow outlined in Fig. 1 was followed to statistically quantify the structural components that could be distinguished in the 3D tomographies. First, the greyscale images were numerically rescaled and converted into 8-bit 3D arrays. Although the original image size is presented for qualitative interpretation, a subset of the original data with dimensions 1,000 × 1,000 × 1,000 pixels was cropped from each image for the quantitative analysis to reduce the computational expense when producing statistically meaningful results.

Image Preprocessing

After cropping the image volume, the initial preprocessing comprised of filtering greyscale images to reduce the noise levels and mitigate, to some extent, the artifacts from reconstruction. Two image filters were selected interactively depending on their effectiveness with noise reduction for each data set; that is, either a Gaussian Blur filter or a bilateral filter was used. The selection was assessed visually. The Gaussian blur filter is a convolution filter for smoothing and has the significant advantage that the filter template is weighted toward the center of the filtered volume.

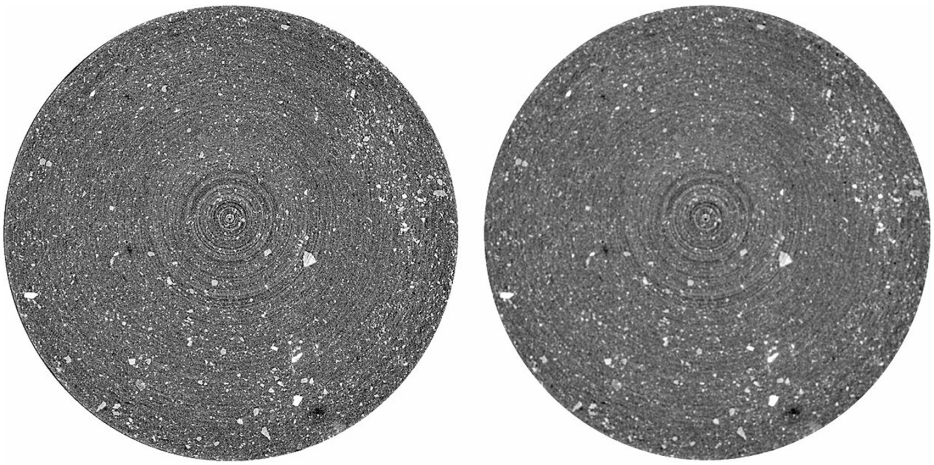

Fig. 2. Effective noise reduction filtering in image (b), in comparison to the original image (a).

An example of the effectiveness of the Gaussian blur filter is indicated in Fig. 2. The bilateral filter is another nonlinear filter for which the intensity magnitude of a pixel is based on the weighted average of the intensities in the neighboring pixels. The bilateral filter yields smooth image data for further processing and preserves the edges of the particles.

However, to be noted is that filtering was not sufficiently effective to improve the signal-to-noise ratio and remove beam hardening artifacts in the microtomography scan at a 20X magnification with a 0.3-μm pixel size. Therefore, the 20X data are only considered in the qualitative analysis.

Segmentation

Image segmentation was used to identify groups of objects and obtain their geometrical properties. The first step in the segmentation procedure is the binarization—the transformation of the greyscale image to a black and white binary image—for which intensity levels lower and higher than a certain threshold value are respectively set to black (0) or white (1) (Fig. 3). In the present research, the threshold value is manually picked for each data set when inspecting the resulting binarized image stack.

The watershed algorithm is a classical method for image segmentation and the creation of unique labels for each individual grain. Consequently, geometrical properties, such as volume, shape, and particle size, as well as the definition of the particle orientation (linked to a reference system) can be quantified for further statistical analyses. In this workflow, the SimpleITK library (Beare et al. 2018) called from the **S**oftware for the **P**ractical **A**nalysis of **M**aterial -***spam***- toolkit version 0.5 (Stamati et al. 2020) was used for the image segmentation and subsequent labeling. Furthermore, before further analyses, the labeled images were corrected for oversegmentation to prevent the overestimation of local maxima in a single grain that typically leads to multiple labels in very large grains. This oversegmentation algorithm detects overly long contacts and merges the labels that share those contacts. In addition, the labels that crossed the boundaries of the image were removed because of their complete geometry and, hence, the associated statistics are unknown. Finally, in the last step, a screening filter removed all labels with (particle) volume <200 pixels because those small particles are sensitive to segmentation artifacts that skew the subsequent analyses. The final result after all image processing steps is presented in Fig. 4 for a slice from the nanotomography.

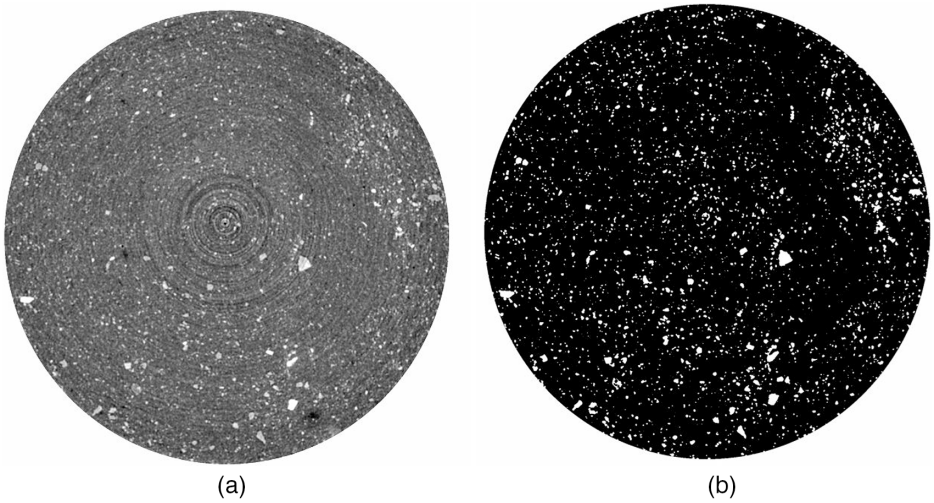

Fig. 3. Binary image (b) after thresholding the original greyscale image (a).

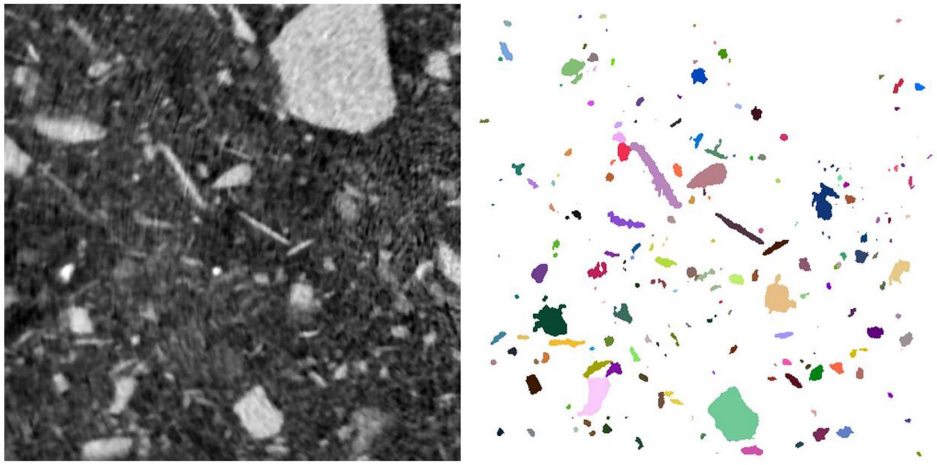

Fig. 4. Labelled image (b) of the original greyscale image (a). All labels crossing boundaries of the image falling below 200 pixels volume were removed.

Fabric Extraction

The metrics used to characterize the fabric from the labeled data were as follows: (1) particle size, (2) particle shape, and (3) particle orientation. An approximate indication of the particle size is given by computing the "equivalent radius," that is, the radius of the sphere with the same volume as the identified particle. Furthermore, the half-axes (a, b, c) of the equivalent ellipsoid corresponding to the particle's moment of inertia were calculated. Although the equivalent radius was used to plot the particle size distribution of the segmented particles, the elliptical geometry was used to determine the aspect ratio of the particles, defined as the ratio of the major and the minor half-axes. The first eigenvector of the moment of inertia is the vector perpendicular to the plane of the maximum moment of inertia and was chosen as the measure for the distribution of the particle orientations. The plotting of 3D orientations uses the Lambert azimuthal equal area projection (Fig. 5) for which an isotropic distribution of angles is projected as equally filling the projected space. This is presented both by plotting the individual points and the binned orientations in a contour plot, as observed in Fig. 5. The advantages of the Lambert projection for particle orientation were presented by Wiebicke et al. (2020).

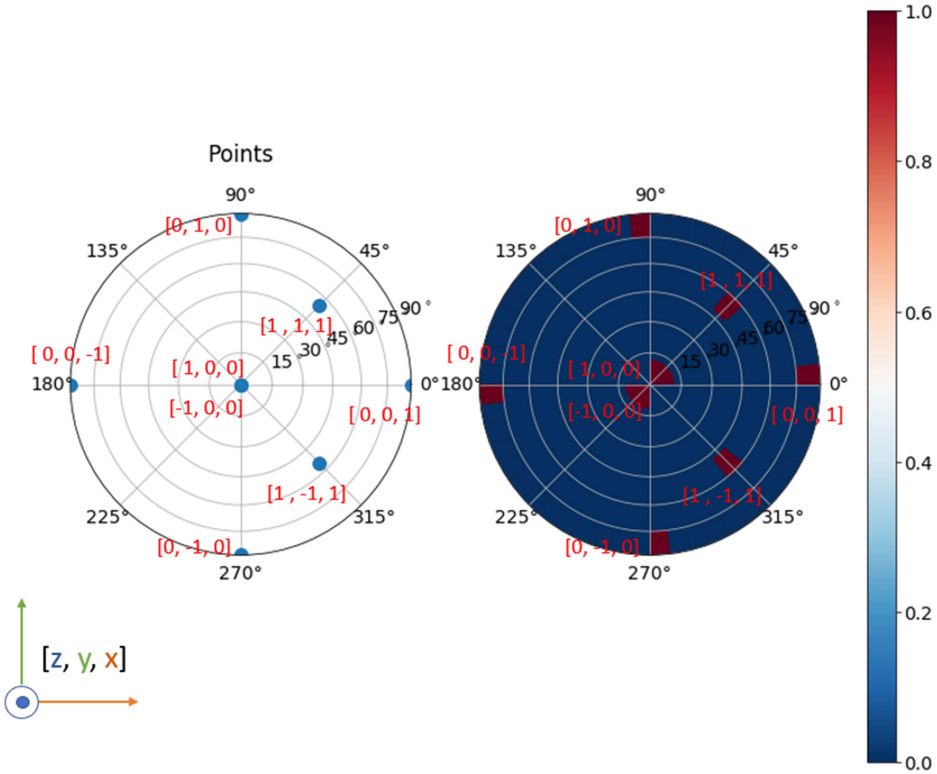

Fig. 5. Elaboration of Lambert projection. Unit vectors are plotted as points or bins, respectively.

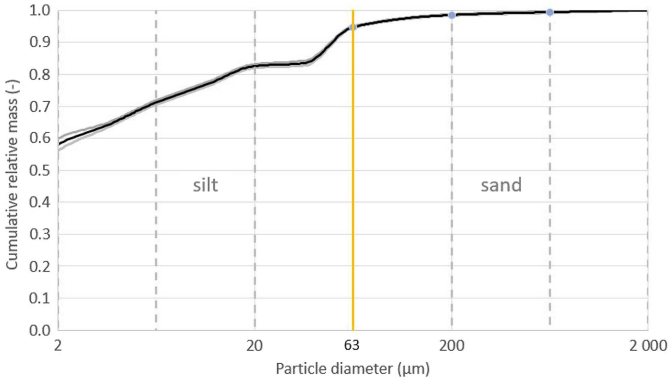

Fig. 6. Particle size distribution of Utby clay (6-m depth) from ISP method. The grey band corresponds to uncertainties of method at small particle sizes.

Results

Basic Characterization Using ISP Method and DLS

The particle size distribution of the natural sensitive clay sampled from a 6-m depth at the Utby test site in Sweden, determined using the ISP method, is indicated in Fig. 6. The mass percentage of clay-sized particles, defined as particles with a size smaller than 2 μm is nearly 60%, with an additional 35% of the particle sizes falling within the silt fraction and a remaining 5% of larger sand grains. This initial characterization by size is in line with the classification based on the plasticity index ($w_p = 18\%–42\%$) and liquid limit ($w_L = 52\%–63\%$) found for samples from this test site in the same depth range (Karlsson et al. 2016). In these sensitive clays, the natural water content is also higher than the liquid limit at $w_N = 69\%–81\%$, leading to a clay classification that falls close to the A-line in the plasticity chart. Thus, depending on the amount of silt in the particular sample, the material is either classified as high plasticity clay CH or high plasticity silt MH following BS 5930:2015.

The clay fraction that did not fully sediment in the ISP test—the supernatant—is studied further using DLS. As described in the methods section, two samples were tested—a direct measurement after diluting the sample and the supernatant that is first filtered with a 2.5-μm filter. The results are indicated in Figs. 7(a and b). Three traces are presented—intensity, volume, and number weighted—that each represents a different frequency distribution correlated from the scattering data.

Clearly, a large number of nano particles with a peak at 170 nm was detected [Fig. 7(a)]. The larger particles that are prominently revealed in the volume and intensity weighted results of the unfiltered sample indicate that only a few large particles skew the correlation. After filtering with the 2.5-μm filter, the results indicate a consistent interpretation with all three correlations leading to a peak that agrees well, resulting in a hydrodynamic diameter of 450 nm [Fig. 7(b)].

Qualitative Interpretation of the Image Data

Representative slices from the reconstructed nano- and microtomography scans on the clay in its natural saturated state are indicated in Fig. 8 (micro) and Fig. 9 (nano), respectively. Fig. 8 indicates the middle slice at three different magnifications for the same sample, that is, leading to a scale of 6.5, 1.3, and 0.3 μm per pixel in each image. The nanoscan in Fig. 9 presents the data for a different sample (from the same site and depth) at 25 nm per pixel. All slices correspond to the horizontal cross section with the out-of-plane direction of the vertical axis (gravity vector) in which the samples are originally deposited and consolidated.

What stands out in all slices of Fig. 8 is the natural speckle arising from the high number of larger, more angular particles embedded in the clay matrix (high image intensities) regardless of magnification. Given that those particles appear at all magnifications, and the natural clay geologically is postglacial, the size range of these particles appears to be large. The fact that these particles are easily discerned in the tomography data leads to the interpretation that these are solid silt grains, sometimes denoted as "rock flour" when the diameter falls to less than 2 μm (e.g., Brand and Brenner 1981), and not agglomerations of clay platelets that have intra and interparticle water (Mitchell and Soga 2005). Substantially more particles are discerned in the nanotomography data indicated in Fig. 9(a), and still further quantification is required to determine whether these particles fall in the 450 nm size range, as determined from DLS. Furthermore, the close-up presented in Fig. 9(b) indicates an underlying clay structure connecting the particles on the threshold of detection.

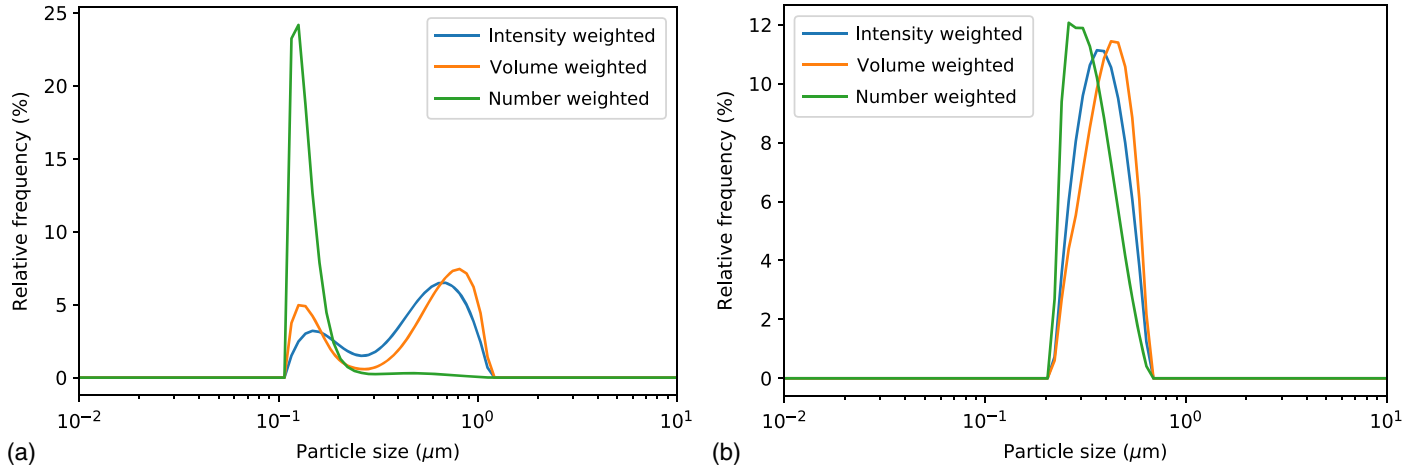

Fig. 7. Results from dynamic light scattering on supernatant from sedimentation test on Utby clay from 6-m depth. Results from unfiltered and filtered (2.5-μm filter) diluted supernatant samples are presented.

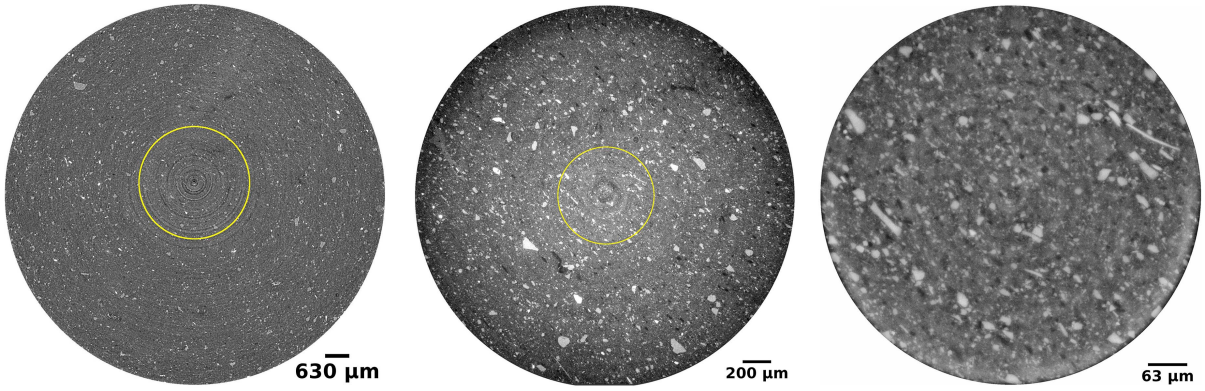

Fig. 8. Reconstructed horizontal cross section from microtomography scan at three different magnifications on single sample of Utby clay. The superimposed circle denotes location of subsequent scan at higher magnification. The high-resolution scan has local contrast enhancing filter applied.

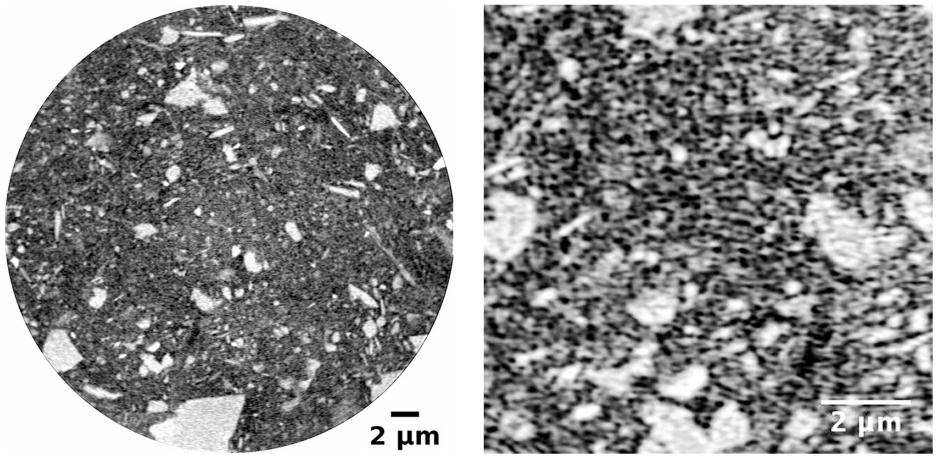

Fig. 9. Reconstructed horizontal cross section from nanotomography scan on Utby clay with original size and image contrast and zoom of 10×10 μm area with enhanced local contrast to showcase structure arising from clay particles.

The pore space visible in Fig. 8 by the black spots with low intensity is most probably linked to the macropore structure of natural sensitive clays (e.g., Delage 2010). Only the nanoscale data appears to indicate a (clay) particle assembly comprised of small and larger particles that form the pore space. Although the speckle representing the clay platelets can be discerned in the data, individual clay platelets are not identified. The average intensity in these speckled grey clay areas found throughout the image is higher than that of the pore space, thus indicating that smaller particles are in the system that are only partially resolved.

SEM imaging was utilized to verify the information on the particle shapes and dimensions as well as the expected emerging fabric. Fig. 10 presents the SEM images at three magnifications of Utby clay (from the same site and depth as the other samples). Larger angular particles are dispersed in a matrix of smaller fine-grained particles that range from submillimeter to submicron in size. Generally, the tomography data presents a 3D view of the microstructure discerned in the 2D SEM data (Fig. 10), although in saturated undisturbed conditions, enabling the monitoring of changes in microstructure.

Quantitative Interpretation of Tomography Data

The spatial resolution of the imaging instrument is not equal to the resolution of the detector used because it also depends on the other components in the acquisition (e.g., scintillator, optics) and the image processing chain. Hence, in the following, the highest spatial resolution achieved in this series of experiments is empirically determined to be around 200 nm because that is the smallest particle size that could be reliably identified from the nanotomography data using the image processing techniques discussed herein. First, the results are presented for each magnification level for which the image processing workflow led to reliably labeled images—low and mid resolution microtomography data and the nanotomography data—that are respectively presented in Figs. 11–13. Each figure presents the cumulative frequency distribution of the number of particles of a certain size; therefore, it is not directly comparable with a typical PSD determined by mass. Furthermore, this relative measure is bounded by the number and size of the particles detected in the subvolume. The particles not detected at a low magnification might be picked up at the next magnification level. The second plot in each figure provides the Lambert projection of the orientation of

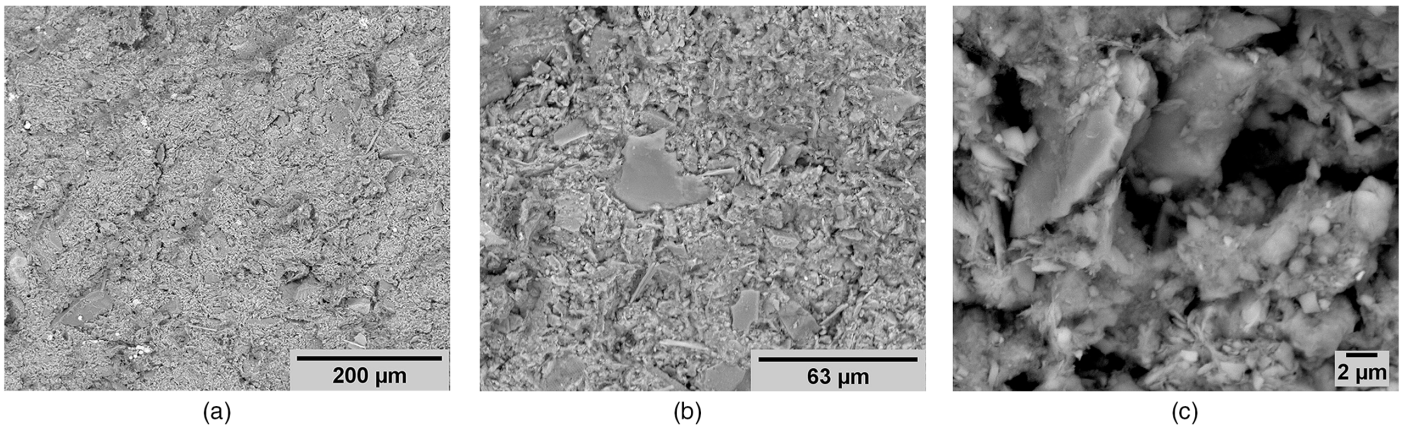

Fig. 10. SEM images of freeze-dried Utby clay (6-m depth) at three magnifications: (a) 422X: low magnification; (b) 1463X: mid magnification; and (c) 9025X: high magnification.

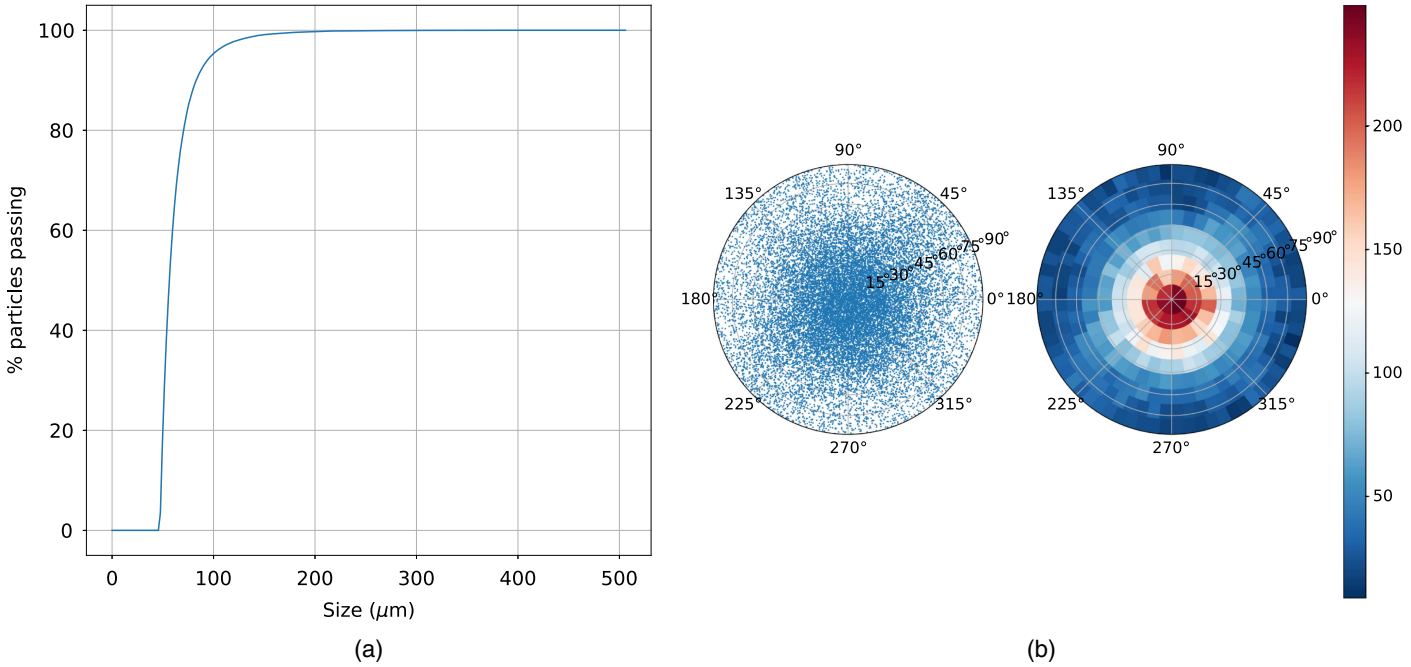

Fig. 11. Frequency distribution and 3D orientation map as determined from segmented and labeled low resolution image data (6.5 μm pixel size, smallest segmented particle has equivalent diameter of ca. 50 μm).

the first eigenvector of each labeled particle and a binned version, as elaborated in Fig. 5.

Starting with the low resolution microtomography data in Fig. 11, the particles with a size range in the silt fraction are uniformly distributed [Fig. 11(a)] with a primarily vertically aligned eigenvector that represents horizontal particle orientations for all particles [Fig. 11(b)]. These larger particles are dispersed in the clay matrix with an orientation commensurate with a horizontally layered deposition and a subsequent vertical consolidation history.

The trend observed in the low resolution data is largely repeated for the processed data from the microtomography at the middle resolution with 1.3 μm per pixel. The particle sizes labeled within this data ranges between 10 and 80 μm, that is, almost the complete span for the silt range [Fig. 12(a)]. A closer look at the particle orientations plotted in Fig. 12(b) reveals that, although mainly horizontally aligned compared with the larger grains in Fig. 11(b), a distinct number of grains are orientated at an angle from the horizontal plane. A visual inspection of the raw data suggests that a local patch of neighboring particles is equally aligned. The origin of this alignment is unclear because it could be both of geological origin or induced by the stress history from (sub)sampling in the testing procedure.

The nanotomography data offer a substantial improvement on the other image data in terms of spatial resolution. Fig. 13(a) indicates that particles as small as 200 nm are detected. The upper band of the size range quantified is 3 μm. Thus, in a traditional size-based characterization, all particles in the labeled set fall within the clay fraction. Furthermore, the mean size at 50% particles passing in Fig. 13(a) coincides with the DLS data at 450 nm. This finding confirms the accuracy of the segmentation and imaging method and questions the ability of the DLS method to pick up on the size of clay platelets with a high aspect ratio. In contrast, the particle orientations have more bias in a single direction around 20° [Fig. 13(b)], which was also observed in the mid resolution data in Fig. 12(b). The small

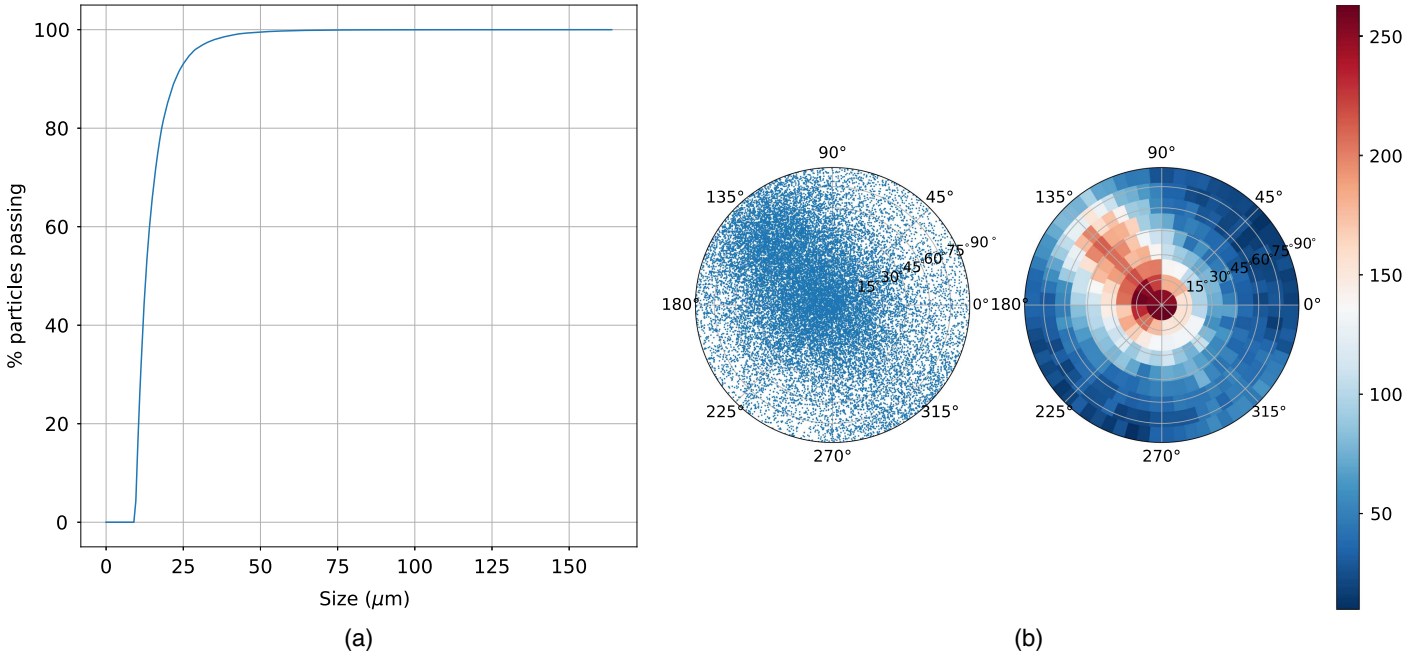

Fig. 12. Frequency distribution and 3D orientation map as determined from segmented and labeled middle resolution image data (1.3 μm pixel size, smallest segmented particle has equivalent diameter of ca. 10 μm).

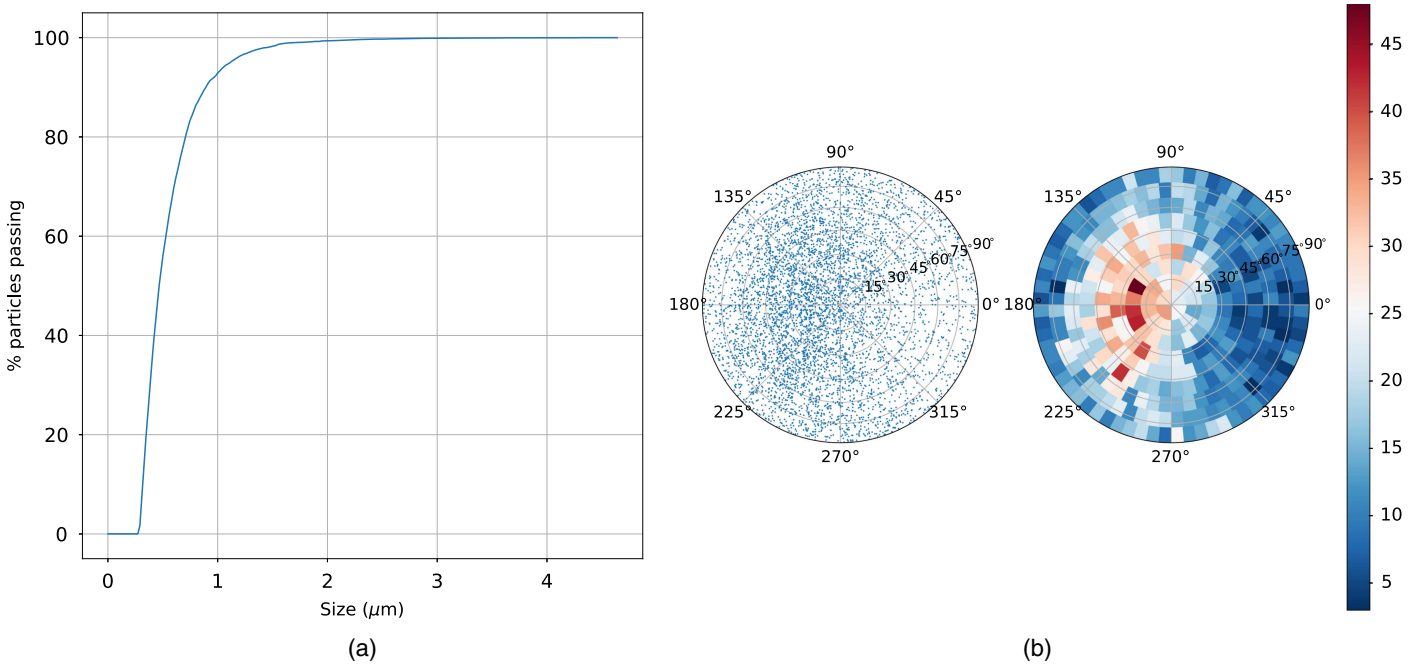

Fig. 13. Frequency distribution and 3D orientation map as determined from segmented and labeled nano image data (25 nm pixel size, smallest segmented particle has equivalent diameter of ca. 200 nm).

particle sizes appear to be much less affected by the consolidation process that otherwise leads to horizontally particle alignments in the larger size fractions.

Discussion

Across magnification levels, image segmentation loses a substantial number of unidentifiable particles: partial particles, smaller silt particles, and clay platelets. The estimated particle fraction by volume of the segmented particles (calculated by dividing the sum of the volume of the segmented particles by the total volume of the segmented image) is 1.42% for the low resolution microtomography and 3.94% for the mid resolution. In the best case—the nano data—only 8% of the volume is characterized, which demonstrates the challenge of imaging clays in their natural saturated state for subsequent quantification.

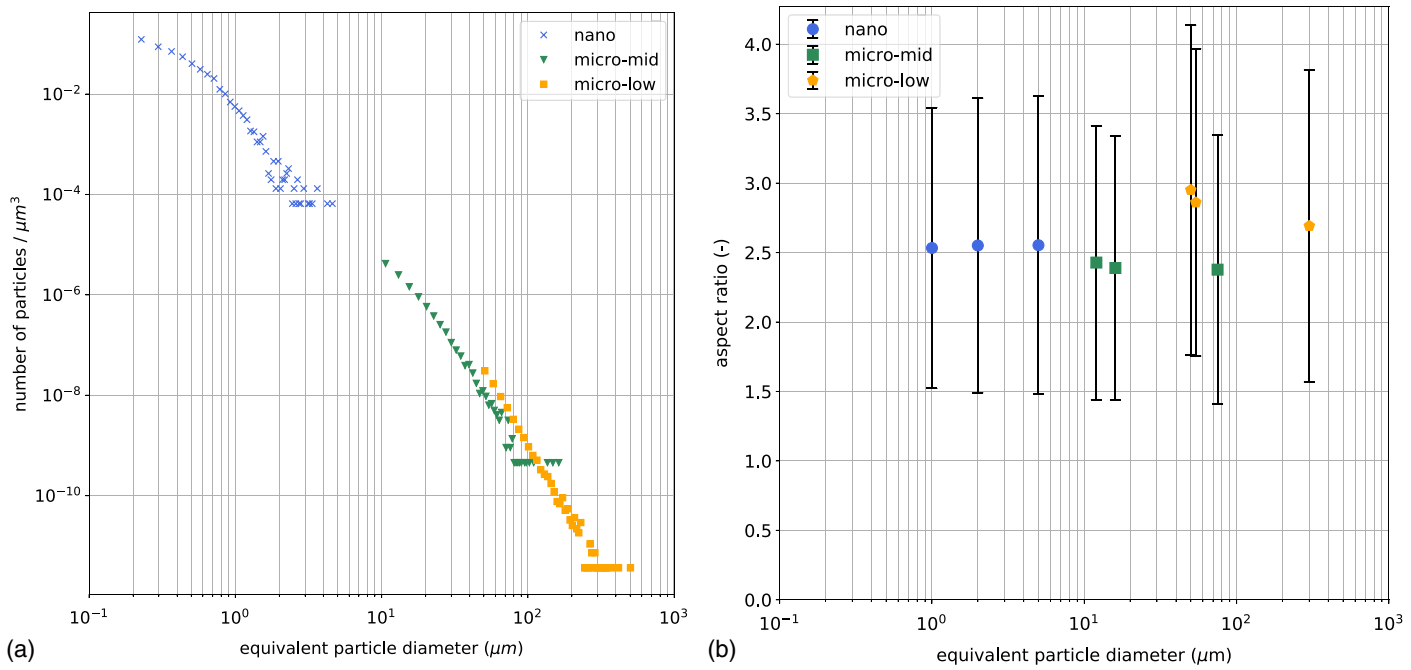

Fig. 14. Detected particle sizes per measurement volume and particle aspect ratio as function of equivalent particle size. For the latter, error bars correspond to standard deviation, and upper bin size is used for plotting on horizontal axis.

Fig. 14(a) presents a more detailed view of the fraction of detected particles per μm^3. A log-log trend of the number of particles as a function of particle size is observed throughout the scales for this natural clay. Furthermore, the consistency in the method for the microtomography data at different magnifications on the same sample is also demonstrated by the close correspondence between the results when they overlap.

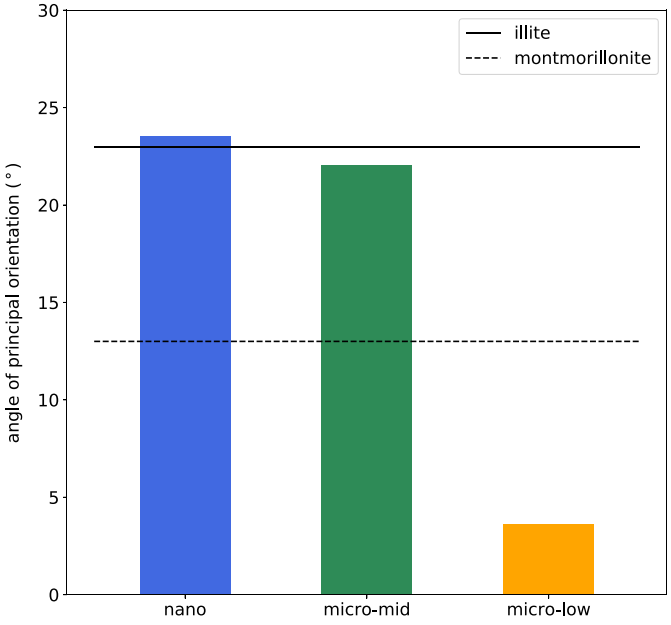

Fig. 15. Mean angle of principal particle orientation for three labeled volumes. Angle represents deviation from horizontal direction. Values for clay particle orientations from SAXS are included for reference. (Data from Birmpilis et al. 2019.)

The type of particles identified across all scales is investigated further by plotting the aspect ratio of the 3D particle shapes as a function of the equivalent particle diameter in Fig. 14(b). In this figure, the mean and standard deviation of the aspect ratio is calculated for three equally sized bins of each data set [based on the frequency distribution reported in Figs. 11(a), 12(a), and 13(a)]. The bin ranges were selected such that three bins of near equal number of particles are created: 47–50, 50–54, and 54–300 μm for low resolution microtomography; 5–12, 12–16, and 16–75 μm for mid resolution microtomography; and 0–1, 1–2, and 2–52 μm for nanotomography.

The results of the aspect ratio summarized in Fig. 14(b) indicate that the aspect ratio is 2.5 ± 1 for the size ranges considered in the statistics, that is, 1–300 μm bins. Therefore, the particles identified are not clay platelets, illite or otherwise, that were reported to have aspect ratios larger than 20 (Mitchell and Soga 2005; Weber et al. 2014). Rather, inert particles that are only mechanically weathered and that have a uniform aspect ratio are identified across all length scales.

The particle orientations identified are largely horizontal, with a distinct alignment direction in higher resolution data. The mean principal particle orientations with reference to the horizontal plane are calculated for each data set to compare this finding with that of prior studies on particle orientations determined using SAXS in natural clay samples from the same test site and depth (Birmpilis et al. 2019). The results, plotted in Fig. 15, indicate that the orientations determined from the image data for small particle sizes, that is, <80 μm, fall near the upper band found for the clay fractions in Utby clay. The illite mineral indicated systematically larger deviations from the horizontal plane than montmorillonite.

Conclusions

Given the current state-of-the-art in imaging and postprocessing, the ability to extract the mean and 3D orientations, size distribution,

and aspect ratios of the mechanically weathered grains across a very wide range of particle sizes, that is, 0.2–300 μm, was demonstrated for a Swedish sensitive clay in its natural saturated state. The measured aspect ratios fall in the range of 2.5 ± 1; hence, the particles identified are not clay platelets, illite or otherwise. Although larger size fractions <80 μm align horizontally—perpendicular to the direction of deposition—the smaller particles are inclined. The persistent 22°–23° deviation in orientation from the horizontal plane for the smaller particle sizes <80 μm agrees well with the inclination found for the clay minerals using SAXS. Furthermore, the measured mean particle size in the nano data of 450 nm corresponds well with the independent determination of particle sizes from dynamic light scattering (DLS). Finally, although the speckle arising from clay particles can be qualitatively discerned in the nanotomography data, the individual platelet-shaped clay particles cannot be segmented for subsequent labeling based on the processing of the fabric properties.

Data Availability Statement

All of the data or code that support the findings of this study are available from the corresponding author on reasonable request.

Acknowledgments

We would like to acknowledge the ESRF grants ma3227 and ma3735 for the beam time at ID19 and support for this series of experiments. Furthermore, we would like to thank Jaime Segura-Ruiz for supporting this project and ID16B beamline for in-house beamtime access. Financial support from the Swedish Research Council (Vetenskapsrådet) under Grant No. 491401, FORMAS under Grant No. 2016-01070, and Trafikverket in the framework Branschsamverkan i Grunden are greatly acknowledged. GB acknowledges the financial support for the experimental campaign from Chalmersska forskningsfonden. The short duration visitor grant from TEC-21 that enabled the collaboration that led to these experiments is acknowledged. Finally, the work presented herein is part of the activities within the International Research Centre for Clay Micromechanics: https://www.irccm.net/.

References

Abed, A. A., and W. T. Sołowski. 2020. "Estimation of water retention behaviour of bentonite based on mineralogy and mercury intrusion porosimetry tests." *Géotechnique* 71 (6): 494–508. https://doi.org/10.1680/jgeot.18.P.220.

Bathurst, R. J., and L. Rothenburg. 1990. "Observations on stress-force-fabric relationships in idealized granular materials." *Mech. Mater.* 9 (1): 65–80. https://doi.org/10.1016/0167-6636(90)90030-J.

Beare, R., B. Lowekamp, and Z. Yaniv. 2018. "Image segmentation, registration and characterization in R with SimpleITK." *J. Stat. Software* 86 (8): 1–35. https://doi.org/10.18637/jss.v086.i08.

Birmpilis, G. 2020. "Multi-scale fabric evolution during hydro-mechanical probing of fine-grained soils." Ph.D. thesis, Dept. of Architecture and Civil Engineering, Chalmers Univ. of Technology.

Birmpilis, G., S. A. Hall, S. Lages, and J. Dijkstra. 2019. "Monitoring of the nano-structure response of natural clay under mechanical perturbation using small angle X-ray scattering and digital image correlation." *Acta Geotech.* 14 (6): 1965–1975. https://doi.org/10.1007/s11440-019-00832-8.

Boller, E., et al. 2017. "Synchrotron-tomography with micro, nano and high temporal resolution for industrial and academic use." In *Proc., ICTMS*. Göttingen, Germany: Copernicus Gesellschaft mbH.

Brand, E. W., and R. P. Brenner. 1981. *Soft clay engineering*. Amsterdam, Netherlands: Elsevier.

Burland, J. 1990. "On the compressibility and shear strength of natural clays." *Géotechnique* 40 (3): 329–378. https://doi.org/10.1680/geot.1990.40.3.329.

Cloetens, P., W. Ludwig, J. Baruchel, D. Van Dyck, D. Van Landuyt, J. P. Guigay, and M. Schlenker. 1999. "Holotomography: Quantitative phase tomography with micrometer resolution using hard synchrotron radiation x rays." *Appl. Phys. Lett.* 75 (19): 2912–2914. https://doi.org/10.1063/1.125225.

Cotecchia, F., S. Guglielmi, F. Cafaro, and A. Gens. 2019. "Characterisation of the multi-scale fabric features of high plasticity clays." *Géotech. Lett.* 9 (4): 361–368. https://doi.org/10.1680/jgele.18.00230.

Deirieh, A., I. Y. Chang, M. L. Whittaker, S. Weigand, D. Keane, J. Rix, J. T. Germaine, D. Joester, and P. B. Flemings. 2018. "Particle arrangements in clay slurries: The case against the honeycomb structure." *Appl. Clay Sci.* 152 (Feb): 166–172. https://doi.org/10.1016/j.clay.2017.11.010.

Delage, P. 2010. "A microstructure approach to the sensitivity and compressibility of some Eastern Canada sensitive clays." *Géotechnique* 60 (5): 353–368. https://doi.org/10.1680/geot.2010.60.5.353.

Delage, P., and G. Lefebvre. 1984. "Study of the structure of a sensitive Champlain clay and of its evolution during consolidation." *Can. Geotech. J.* 21 (1): 21–35. https://doi.org/10.1139/t84-003.

Delage, P., and D. Tessier. 2021. "Macroscopic effects of nano and microscopic phenomena in clayey soils and clay rocks." *Geomech. Energy Environ.* 27 (Sep): 100177. https://doi.org/10.1016/j.gete.2019.100177.

Djéran-Maigre, I., D. Tessier, D. Grunberger, B. Velde, and G. Vasseur. 1998. "Evolution of microstructures and of macroscopic properties of some clays during experimental compaction." *Mar. Pet. Geol.* 15 (2): 109–128. https://doi.org/10.1016/S0264-8172(97)00062-7.

Dor, M., Y. Levi-Kalisman, R. J. Day-Stirrat, Y. Mishael, and S. Emmanuel. 2020. "Assembly of clay mineral platelets, tactoids, and aggregates: Effect of mineral structure and solution salinity." *J. Colloid Interface Sci.* 566 (Apr): 163–170. https://doi.org/10.1016/j.jcis.2020.01.084.

Durner, W., S. C. Iden, and G. von Unold. 2017. "The integral suspension pressure method (ISP) for precise particle-size analysis by gravitational sedimentation." *Water Resour. Res.* 53 (1): 33–48. https://doi.org/10.1002/2016WR019830.

Fonseca, J., C. Sullivan, M. R. Coop, and P. Lee. 2013. "Quantifying the evolution of soil fabric during shearing using directional parameters." *Géotechnique* 63 (6): 487–499. https://doi.org/10.1680/geot.12.P.003.

Gee, G., and D. Or. 2002. "2.4 particle-size analysis." In *Methods of soil analysis*. Hoboken, NJ: Wiley.

Giesche, H. 2006. "Mercury porosimetry: A general (practical) overview." *Part. Part. Syst. Charact.* 23 (1): 9–19. https://doi.org/10.1002/ppsc.200601009.

Glatter, O., and O. Kratky. 1982. *Small angle X-ray scattering*. London: Academic Press.

Hattab, M., and J.-M. Fleureau. 2011. "Experimental analysis of kaolinite particle orientation during triaxial path." *Int. J. Numer. Anal. Methods Geomech.* 35 (8): 947–968. https://doi.org/10.1002/nag.936.

Hattab, M., T. Hammad, J.-M. Fleureau, and P.-Y. Hicher. 2013. "Behaviour of a sensitive marine sediment: Microstructural investigation." *Géotechnique* 63 (1): 71–84. https://doi.org/10.1680/geot.10.P.104.

Hemes, S., G. Desbois, J. L. Urai, B. Schröppel, and J.-O. Schwarz. 2015. "Multi-scale characterization of porosity in Boom Clay (HADES-level, Mol, Belgium) using a combination of X-ray -CT, 2D BIB-SEM and FIB-SEM tomography." *Microporous Mesoporous Mater.* 208 (May): 1–20. https://doi.org/10.1016/j.micromeso.2015.01.022.

Hicher, P. Y., H. Wahyudi, and D. Tessier. 2000. "Microstructural analysis of inherent and induced anisotropy in clay." *Mech. Cohesive-frict. Mater.* 5 (5): 341–371. https://doi.org/10.1002/1099-1484(200007)5:5<341::AID-CFM99>3.0.CO;2-C.

Imseeh, W. H., A. M. Druckrey, and K. A. Alshibli. 2018. "3D experimental quantification of fabric and fabric evolution of sheared granular materials using synchrotron micro-computed tomography." *Granular Matter* 20 (2): 1–28. https://doi.org/10.1007/s10035-018-0798-x.

ISO. 2017. *2017 Particle size analysis—Dynamic light scattering (DLS)*. ISO 22412:2017. Geneva: IOS.

Karlsson, M., A. Emdal, and J. Dijkstra. 2016. "Consequences of sample disturbance when predicting long-term settlements in soft clay." *Can. Geotech. J.* 53 (12): 1965–1977. https://doi.org/10.1139/cgj-2016-0129.

Ken-Ichi, K. 1984. "Distribution of directional data and fabric tensors." *Int. J. Eng. Sci.* 22 (2): 149–164. https://doi.org/10.1016/0020-7225(84)90090-9.

Kuhn, M. R., W. Sun, and Q. Wang. 2015. "Stress-induced anisotropy in granular materials: Fabric, stiffness, and permeability." *Acta Geotech.* 10 (4): 399–419. https://doi.org/10.1007/s11440-015-0397-5.

Leroueil, S., and P. Vaughan. 1990. "The general and congruent effects of structure in natural soils and weak rocks." *Géotechnique* 40 (3): 467–488. https://doi.org/10.1680/geot.1990.40.3.467.

Martínez-Criado, G., et al. 2016. "ID16B: A hard X-ray nanoprobe beamline at the ESRF for nano-analysis." *J. Synchrotron Radiat.* 23 (1): 344–352. https://doi.org/10.1107/S1600577515019839.

Mirone, A., E. Brun, E. Gouillart, P. Tafforeau, and J. Kieffer. 2014. "The PyHST2 hybrid distributed code for high speed tomographic reconstruction with iterative reconstruction and a priori knowledge capabilities." *Nucl. Instrum. Methods Phys. Res., Sect. B* 324 (Apr): 41–48. https://doi.org/10.1016/j.nimb.2013.09.030.

Mitchell, J. K., and K. Soga. 2005. Vol. 3 of *Fundamentals of soil behavior*. New York: Wiley.

Oda, M., and J. Konishi. 1974. "Microscopic deformation mechanism of granular material in simple shear." *Soils Found.* 14 (4): 25–38. https://doi.org/10.3208/sandf1972.14.4_25.

Paganin, D., S. C. Mayo, T. E. Gureyev, P. R. Miller, and S. W. Wilkins. 2002. "Simultaneous phase and amplitude extraction from a single defocused image of a homogeneous object." *J. Microsc.* 206 (1): 33–40. https://doi.org/10.1046/j.1365-2818.2002.01010.x.

Pusch, R. 1970. "Clay microstructure. A study of the microstructure of soft clays with special reference to their physical properties." In *Proc., No. 24*. Stockholm, Sweden: Swedish Geotechnical Institute.

Ringdal, N., D. D. M. Fonseca, E. Hansen, H. Hemmen, and J. Fossum. 2010. "Nematic textures in colloidal dispersions of na-fluorohectorite synthetic clay." *Phys. Rev. E* 81 (4): 041702. https://doi.org/10.1103/PhysRevE.81.041702.

Rorato, R., M. A. A. de Toledo, E. C. G. Andò, A. Gens, and G. Viggiani. 2020. "Linking shape and rotation of grains during triaxial compression of sand." *Granular Matter* 22 (4): 1–21. https://doi.org/10.1007/s10035-020-01058-2.

Santamarina, J. C. 2003. "Soil behavior at the microscale: Particle forces." In *Proc., Symp. Soil Behavior and Soft Ground Construction, in Honor of Charles C. Ladd*, 25–56. Cambridge, MA: Geo-Institute of ASCE.

Schindelin, J., et al. 2012. "Fiji: An open-source platform for biological-image analysis." *Nat. Methods* 9 (7): 676–682. https://doi.org/10.1038/nmeth.2019.

Schuck, B., G. Desbois, and J. L. Urai. 2020. "Grain-scale deformation mechanisms and evolution of porosity in experimentally deformed boom clay." *J. Struct. Geol.* 130 (Jan): 103894. https://doi.org/10.1016/j.jsg.2019.103894.

SIS (Swedish Institute for Standards). 2012. *Sludge, treated biowaste, soil and waste—Determination of loss on ignition*. SS-EN 15935:2012. Stockholm, Sweden: SIS.

SIS (Swedish Institute for Standards). 2020. *Soil quality—Determination of particle size distribution in mineral soil material—Method by sieving and sedimentation*. SS-ISO 11277:2020. Stockholm, Sweden: SIS.

Stamati, O., et al. 2020. Spam: Software for practical analysis of materials." *J. Open Source Software* 5 (51): 2286. https://doi.org/10.21105/joss.02286.

Stavropoulou, E., E. Andò, E. Roubin, N. Lenoir, A. Tengattini, M. Briffaut, and P. Bésuelle. 2020. "Dynamics of water absorption in callovo-oxfordian claystone revealed with multimodal X-ray and neutron tomography." *Front. Earth Sci.* 8 (Mar): 6. https://doi.org/10.3389/feart.2020.00006.

Stetefeld, J., S. McKenna, and T. Patel. 2016. "Dynamic light scattering: A practical guide and applications in biomedical sciences." *Biophys. Rev.* 8 (4): 409–427. https://doi.org/10.1007/s12551-016-0218-6.

Suuronen, J.-P., M. Matusewicz, M. Olin, and R. Serimaa. 2014. "X-ray studies on the nano- and microscale anisotropy in compacted clays: Comparison of bentonite and purified calcium montmorillonite." *Appl. Clay Sci.* 101 (Nov): 401–408. https://doi.org/10.1016/j.clay.2014.08.015.

Toer, P. A., and L. Reimer. 1998. *Scanning electron microscopy: Physics of image formation and microanalysis*. Berlin: Springer.

Viggiani, G., N. Lenoir, P. Bésuelle, M. Di Michiel, S. Marello, J. Desrues, and M. Kretzschmer. 2004. "X-ray microtomography for studying localized deformation in fine-grained geomaterials under triaxial compression." *C.R. Méc.* 332 (10): 819–826. https://doi.org/10.1016/j.crme.2004.05.006.

Wang, R., Y. F. Dafalias, P. Fu, and J.-M. Zhang. 2020. "Fabric evolution and dilatancy within anisotropic critical state theory guided and validated by DEM." *Int. J. Solids Struct.* 188 (Apr): 210–222. https://doi.org/10.1016/j.ijsolstr.2019.10.013.

Wang, S., Z. J. Yang, and P. Yang. 2017. "Structural change and volumetric shrinkage of clay due to freeze-thaw by 3D X-ray computed tomography." *Cold Reg. Sci. Technol.* 138 (Jun): 108–116. https://doi.org/10.1016/j.coldregions.2017.03.007.

Weber, C., M. Heuser, and H. Stanjek. 2014. "A collection of aspect ratios of common clay minerals determined from conductometric titrations." *Clay Miner.* 49 (3): 495–498. https://doi.org/10.1180/claymin.2014.049.3.10.

Wensrich, C., J. Pineda, V. Luzin, L. Suwal, E. Kisi, and H. Allameh-Haery. 2018. "Deformation and fabric in compacted clay soils." *Phys. Rev. Appl.* 9 (5): 054003. https://doi.org/10.1103/PhysRevApplied.9.054003.

Wiebicke, M., E. Andó, G. Viggiani, and I. Herle. 2020. "Measuring the evolution of contact fabric in shear bands with X-ray tomography." *Acta Geotech.* 15 (1): 79–93. https://doi.org/10.1007/s11440-019-00869-9.

Yao, Y., and D. Liu. 2012. "Comparison of low-field NMR and mercury intrusion porosimetry in characterizing pore size distributions of coals." *Fuel* 95 (May): 152–158. https://doi.org/10.1016/j.fuel.2011.12.039.

Yimsiri, S., and K. Soga. 2010. "DEM analysis of soil fabric effects on behaviour of sand." *Géotechnique* 60 (6): 483–495. https://doi.org/10.1680/geot.2010.60.6.483.

Zhao, C., G. Pinzon, M. Wiebicke, E. Andó, G. Viggiani, and N. Kruyt. 2021. "Evolution of fabric anisotropy of granular soils: X-ray tomography measurements and theoretical modelling." *Comput. Geotech.* 133 (May): 104046. https://doi.org/10.1016/j.compgeo.2021.104046.

Zhao, D., Q.-F. Gao, M. Hattab, P.-Y. Hicher, and Z.-Y. Yin. 2020. "Microstructural evolution of remolded clay related to creep." *Transp. Geotech.* 24 (Sep): 100367. https://doi.org/10.1016/j.trgeo.2020.100367.

Zhao, J., and N. Guo. 2013. "Unique critical state characteristics in granular media considering fabric anisotropy." *Géotechnique* 63 (8): 695–704. https://doi.org/10.1680/geot.12.P.040.